J. Phys. B: At. Mol. Opt. Phys. **44** (2011) 135201 (12pp) doi:10.1088/0953-4075/44/13/135201

Dielectronic recombination of heavy species: the tin $4p^64d^q - 4p^64d^{(q-1)}4f + 4p^54d^{(q+1)}$ transition arrays for q = 1–10

N R Badnell[1], A Foster[1,4], D C Griffin[2], D Kilbane[3], M O'Mullane[1] and H P Summers[1]

[1] Department of Physics, University of Strathclyde, Glasgow, G4 0NG, UK
[2] Department of Physics, Rollins College, Winter Park, FL 32789, USA
[3] School of Physics, University College Dublin, Belfield, Dublin 4, Ireland

E-mail: badnell@phys.strath.ac.uk

Received 12 April 2011, in final form 20 May 2011
Published 17 June 2011
Online at stacks.iop.org/JPhysB/44/135201

Abstract

We report on detailed calculations of dielectronic recombination (DR) rate coefficients for Sn^{4+}–Sn^{13+} using three approaches of differing degrees of complexity. These are configuration-mixed Breit–Pauli using the AUTOSTRUCTURE code, bundled-*nl* using the Burgess–Bethe general program (BBGP) and configuration average (CA) using the DRACULA code. We find that target $\Delta n = 0$ dipole promotions dominate the total DR rate coefficients; configuration-mixing effects are small for the totals; results for the totals are highly dependent on the initial levels averaged over—the results for averaging over all levels of the ground configuration being typically nearly a factor of 2 smaller than for using only the ground level. On comparing the total DR rate coefficients obtained using the three methods we find that the BBGP results are systematically lower than those obtained from AUTOSTRUCTURE—in some cases they are significantly lower (by a factor of 2)—while the CA results are systematically and significantly higher (by up to 80%) in general. These findings need to be borne in mind for the finite-density modelling of tin plasma sources for microlithography and tin markers for magnetic fusion plasmas especially when using simple descriptions of DR. They apply also to heavy species in general such as tungsten ions which are of great importance for magnetic fusion plasmas.

(Some figures in this article are in colour only in the electronic version)

1. Introduction

Tin plasmas are a keen interest of study as an extreme ultraviolet (EUV) light source for next-generation microlithography [1]. Usable wavelengths are rather restricted due to mirror absorption, etc. Suitable emission around 13.5 nm is particularly intense from Sn^{7+} through Sn^{12+} ions [2]. It is dominated by the $4p^64d^q - 4p^64d^{(q-1)}4f + 4p^54d^{(q+1)}$ unresolved transition array. Such an arrangement of configurations is subjected to strong configuration-mixing which leads to a spectacular quenching of the unmixed spectra [3, 4]. Modelling such emission requires knowledge of the tin ionization balance. The dominant recombination mechanism is dielectronic. Its accurate description is somewhat demanding due to the complexity of the configurations involved—the open d-subshell targets. The only detailed calculation we can find is on Sn^{10+} [5] which made use of the flexible atomic code (FAC) [6].

Heavy species are also of particular interest to magnetic fusion and especially ITER [7]. A tin-coated probe has been

[4] Present address: Harvard-Smithsonian Center for Astrophysics, 60 Garden Street, Cambridge, MA 02138, USA.

used on the Mega Amp Spherical Tokomak to study heavy species markers for erosion transport diagnostics [8]. The main heavy species for ITER will be tungsten. It is in this context that Ballance *et al* [9] studied the dielectronic recombination (DR) of W^{35+}—which is isoelectronic with Sn^{11+}. They carried out calculations using three different methods, namely Dirac *R*-matrix close-coupling, Breit–Pauli perturbation theory (via the AUTOSTRUCTURE code) and configuration average (CA). The CA total DR rate coefficients were only 10–15% larger than those obtained from perturbation theory while the *R*-matrix ones were $\sim 20\%$ smaller than perturbation theory's. Configuration-mixing was omitted from the level-resolved calculations as it was too demanding computationally. (The CA method 'omits' configuration-mixing fundamentally.) It is of interest to see how well the CA method fares once configuration-mixing is taken into account by the detailed (perturbation theory) calculations. The CA description of DR is very efficient and can be applied easily to all ionization stages of tin and tungsten and can take account of all significant recombination pathways configuration resolved. It is also an improvement over the present modelling usage of average-atom rate coefficients—these were nearly a factor of 2 larger than CA for W^{35+} at typical magnetic fusion plasma temperatures [9].

Recent developments in the AUTOSTRUCTURE code have significantly reduced its memory requirement for complex heavy species [10] and it is now possible to treat DR via the $4p^6 4d^q - 4p^6 4d^{(q-1)} 4f + 4p^5 4d^{(q+1)}$ transition arrays for $q =$ 1–10 in a full configuration-mixed level-resolved Breit–Pauli calculation using kappa-averaged relativistic wavefunctions. This opens up its application more widely to technical, fusion [11] and astrophysical plasmas [12] involving heavy species—which we take to be elements of the periodic table which lie beyond zinc.

It is desirable also to consider an additional approach which falls between the full level-resolved and configuration-averaged ones—the Burgess–Bethe [13]. This approach is the one used by the atomic data and analysis structure (ADAS) [14] for its *baseline* description of DR. The *baseline* approach is the one used for the collisional–radiative modelling of heavy species for magnetic fusion [8]. The Burgess–Bethe method [13] treats DR in an uncoupled representation (between the target and colliding/Rydberg electron) and thus is able to take account of configuration-mixing in the *N*-electron target/core alone. Thus, it is superior to the CA method and much less demanding computationally than the full level-resolved perturbation approach of AUTOSTRUCTURE which describes $(N+1)$-electron configuration-mixing in the DR process. The original implementation in the Burgess–Bethe general program (BBGP) was the basis for the seminal Burgess general formula (GF) [15]. It has undergone significant enhancement to treat 'alternative' pathways [16] which were not described back then.

The outline of the paper is as follows: in section 2, we describe briefly the theory behind the perturbative treatment of DR as it is implemented in the AUTOSTRUCTURE code, the BBGP and the CA; in section 3, we compare results from these three different methods; in section 4, we recapitulate; and in section 5, we draw some conclusions.

2. Theory

The partial DR rate coefficient α^z_{fi} from an initial state i of an ion X^{+z} into a resolved final state f of an ion X^{+z-1} is given by

$$\alpha^z_{fi}(T) = \left(\frac{4\pi a_0^2 I_{\rm H}}{k_{\rm B} T_{\rm e}}\right)^{3/2} \sum_j \frac{\omega_j}{2\omega_i} \, {\rm e}^{-E_{\rm c}/(k_{\rm B} T_{\rm e})} \times \frac{\sum_l A^{\rm a}_{j\to i, E_{\rm c} l} \, A^{\rm r}_{j\to f}}{\sum_h A^{\rm r}_{j\to h} + \sum_{m,l} A^{\rm a}_{j\to m, E_{\rm c} l}} \qquad (1)$$

in the isolated resonance approximation [13]. Here, ω_j is the statistical weight of the $(N+1)$-electron doubly excited resonance state j, ω_i is the statistical weight of the N-electron target state (so $z = Z - N$) and the autoionization ($A^{\rm a}$) and radiative ($A^{\rm r}$) rates are in inverse seconds. $E_{\rm c}$ is the energy of the continuum electron (with orbital angular momentum l) which is fixed by the position of the resonances and $I_{\rm H}$ is the ionization potential energy of the hydrogen atom (both in the same units of energy), $k_{\rm B}$ is the Boltzman constant, $T_{\rm e}$ is the electron temperature and $\left(4\pi a_0^2\right)^{3/2} = 6.6011 \times 10^{-24}$ cm^3.

The spectroscopic modelling of finite-density plasmas requires final-state resolution so as to take account of the collisional redistribution of the final state. This is beyond the scope of this paper and so all of the results that we present are for the total recombination rate coefficient, i.e. summed over all f that are stable against autoionization.

Equation (1) is applicable to all three methods that we consider. The difference lies in the interpretation of the state representation: level resolved, uncoupled parent-plus-electron or configuration.

2.1. Implementation

All three methods include only the electric dipole radiation operator in the DR process. AUTOSTRUCTURE describes arbitrary E_k and M_k multipoles but they are of negligible importance for total DR rate coefficients. All three methods include only the electrostatic operator to describe autoionization. AUTOSTRUCTURE describes both the two-body fine- and non-fine-structure operators of the Breit–Pauli Hamiltonian as well. They can be neglected here.

2.1.1. AUTOSTRUCTURE. The state labels are levels and are readily interpretable in the usual sense. Explicit expressions for the autoionization rate may be found in [17] and the radiative rate in [18].

Calculations were carried out for Rydberg nl up to $n = 100$ and $l = 7$ so as to converge the total DR rate coefficients to $\sim 1\%$. We included the three target configurations of the title which are then coupled to Rydberg and continuum electrons. We also included all $(N+1)$-electron bound-orbital configurations that result from adding an $n = 4$ orbital to the target configurations. This describes outer electron radiation into the core. Radiation from $n \to n' \geqslant 5$ is treated

hydrogenically. This is the only additional approximation to the Breit–Pauli level-resolved isolated resonance approach.

We note that we form the N- and $(N + 1)$-electron interaction Hamiltonians explicitly all the way up to $n = 100$ on making use of the correspondence principle. This enables us to generate autoionization rates for channels which do not open up until high n (e.g. $n = 40$). These autoionizing transitions between fine-structure levels[5] strongly suppress recombination through the high-n states. Extrapolation of autoionization rates from low n (e.g. $n = 15$) omits these channels and can lead to a substantial overestimate of the high-temperature (total) DR rate coefficients. There is a converse effect. If the ground term splits into fine-structure levels, then low-temperature DR can be enhanced significantly by these high-n dielectronic *captures*. It is a highly charged ion effect since the radiative stabilization is by the Rydberg electron to a large set of true bound states built upon excited parents [19].

We use the kappa-averaged relativistic orbital approximation [20] but with a self-consistent CA model potential [21] rather than the Hartree–Fock relativistic (HFR) [20]. The required occupation numbers are the average of the three target configurations with the appropriate self-interaction omitted for each orbital, i.e. the potentials are slightly different for each orbital. The kappa-averaged approach inherently gives rise to non-orthogonal orbitals and so there is nothing to be gained by using a unique model potential. We neglect the small component of the Dirac spinor.

The advantages of this approach are that all possible pathways are described level resolved with full configuration-mixing in both the N- and $(N + 1)$-electron bound orbital configurations. The disadvantage is that it is computationally demanding and so places restrictions on the number of N-electron configurations used to describe the problem. It is largely a memory limitation. Each Rydberg nl is treated separately and the code is already parallel by l. The wall clock time could be reduced further by parallelization in n. The trend of modern computers is towards massive parallelization but with relatively small memory per processor. Node memory is then fully used without full utilization of the available processors.

2.1.2. BBGP. The state labels are target/parent levels uncoupled to the Rydberg/continuum electron in a bundled-nl representation. Explicit expressions for the radiative and autoionization rates may be found in [16]. They are given in terms of an LS-coupling representation but are readily recoupled to LSJ. The use of the Bethe (dipole) approximation for the autoionization rates greatly simplifies equation (1). It reduces the problem to an N-electron description for the radiative rates plus rapidly evaluated hydrogenic bound-free radial integrals. The inaccuracy of the Bethe approximation for low l is overcome through the introduction of 'universal' correction factors. The correction factors and their use have been improved upon over the years. The present BBGP implementation [16] also allows for alternate Auger breakup and parent radiative transition pathways that were not part of the original one by Burgess [13]. A further refinement is possible if (threshold) distorted wave partial collision strengths are available from some external source such as the new development in AUTOSTRUCTURE [10]. Non-dipole autoionization pathways can be described as well then and the dipole rates can use explicit correction factors instead of the 'universal' ones. The present work is restricted to dipole transitions only.

Calculations were carried out to convergence of the Rydberg nl sum (typically to $n = 1000$ and $l = 15$) for both $\Delta n_p = 0$ and $\Delta n_p = 1$ dipole promotions from the initial ground configuration. The bound-state wavefunctions, radiative rates and energies are determined in the HFR approximation [20] using a modified version of the RCN code developed by Cowan [21].

The advantages of the BBGP approach are its ability to determine rapidly the relative contributions from all possible recombination pathways for arbitrary complex ions and its inclusion of N-electron configuration-mixing. Limitations of the BBGP approach are the restriction to dipole autoionizing transitions unless external distorted wave data are available and the neglect of $(N + 1)$-electron configuration-mixing.

2.1.3. CA. The state labels are configurations and so ω_i and ω_j are the total statistical weights of the N- and $(N + 1)$-electron configurations. The CA approximation method referred to here is an *a priori* analytic average. This is not to be confused with the *a posterior* numerical average of term/level-resolved (configuration-mixed) atomic data for subsequent 'CA' modelling. Explicit expressions for the CA rates used here may be found in [22, 23]. The program implementation DRACULA (DR average configuration using local approximation) has been extensively revised recently [9] to handle up to eight open subshells and for a more robust treatment of high-nl rates.

The present calculations were carried out up to $n = 1000$ and $l = 12$. The bound-state wavefunctions and energies are determined in the HFR approximation [20] using a slightly modified version of the latest RCN code (Mod36) developed by Cowan [21].

The main advantage of the CA approach is its ability to determine rapidly the relative contributions from all possible recombination pathways for arbitrary complex ions. Limitations of the approach and/or implementation are as follows: a configuration which straddles the ionization limit must be taken to be either bound or autoionizing, autoionization within a core configuration (e.g. $4d^q nl \rightarrow 4d^q + e^-$) is omitted and configuration-mixing is not represented in any way.

2.2. Configuration-mixing

We demonstrate the strong mixing between the $4p^6 4d^{(q-1)} 4f$ and $4p^5 4d^{(q+1)}$ configurations. We choose to do so for Sn^{10+} ($q = 4$) since it (along with Sn^{11+}) is the strongest emitter [2] around 13.5 nm. Similar effects occur for all q considered here. In figure 1, we show the total line strength emission as a function of wavelength. We have convoluted it with a 0.01 nm

[5] The autoionization interaction itself is still the Coulomb electrostatic.

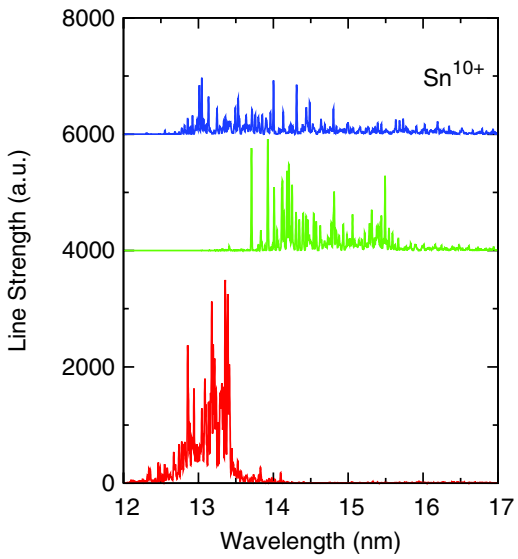

Figure 1. Total line strength emission in Sn^{10+} as a function of the wavelength convoluted with a 0.01 nm FWHM Gaussian. The top spectrum is from the 4p–4d array and the middle one from the 4d–4f array and where each has been calculated separately. The bottom spectrum is the configuration-mixed ($4p^64d^34f$ with $4p^54d^5$) sum of 4p–4d and 4d–4f. See the text for details. All this work.

FWHM Gaussian so as to facilitate comparison. We show the emission from the $4p^64d^34f$ and $4p^54d^5$ configurations calculated separately and from the two mixed. The latter is clearly not a superposition of the former two. The spectral emission has changed dramatically. Such effects have been observed before—in Pr^{21+} for example [4]. It is important to remember that the total line strength emission summed over all wavelengths is unchanged since the only difference between the two sums is a pure unitary transformation. Higher order energy moments would differ somewhat since the differing wavelengths then come into play.

We consider now the implication for DR as described by equation (1). Autoionization rates can be expected to be changed markedly by configuration-mixing in a similar fashion to the radiative rates. This is exemplified by the Bethe approximation as we have noted already. If all autoionizing levels satisfy either $A^{\rm r} \ll A^{\rm a}$ or $A^{\rm r} \gg A^{\rm a}$, then to a first approximation[6] all Auger yields or fluorescence yields are unity. The total DR rate coefficient is unchanged then by the unitary configuration-mixing transformation save for the exponential factor. The exponential is unity at high temperatures. At low temperatures any near threshold autoionizing levels will have their relative position changed dramatically by configuration-mixing within the core. The energy factor then changes exponentially. The change in wavelength in figure 1 is due purely to changes in position of the upper level. The position of the lower levels is unaffected since we consider only electric dipole transitions.

The effect of configuration-mixing on the total DR rate coefficient then depends on the degree to which the above conditions are violated. Individual partial final-state resolved

[6] It also depends on (the sum over) i, f, h and m—see the detailed study by Cowan and Griffin [24] for further details.

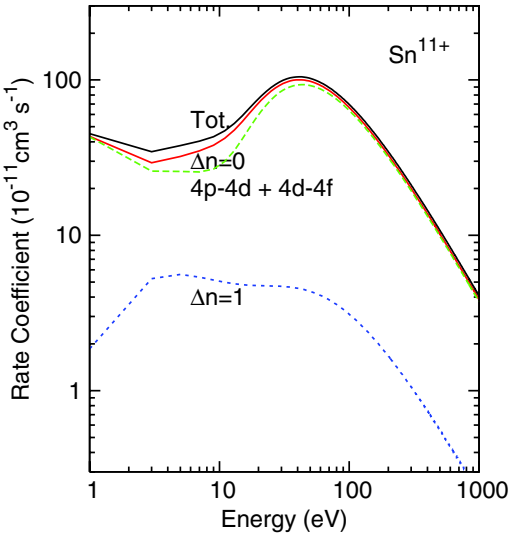

Figure 2. CA DR contributions for Sn^{11+}. $\Delta n = 0$ denotes the sum of the $4l$–$4l'$ contributions and $\Delta n = 1$ denotes the sum of the $4l$–$5l'$. 'Tot.' denotes the sum of the $\Delta n = 0$ and $\Delta n = 1$. See the text for details. All this work.

DR rate coefficients can be expected to change dramatically along the lines illustrated in figure 1. These are necessary for spectral diagnostics and finite-density collisional–radiative modelling.

3. Results

We establish first the dominant contributions to the tin DR rate coefficients using the CA method and then compare and contrast them with the results of our level-resolved calculations. We study Sn^{11+} first since this is isoelectronic with W^{35+} and so we can compare and contrast with the findings of [9]. Next, we look at the lower charge end and the case of Sn^{7+}. We then consider the remaining ions of interest as an EUV light source: Sn^{8+}–Sn^{10+}, Sn^{12+} and Sn^{13+}. The lowest charge $4d^q$ (q = 8–10) Sn ions are also considered since they are of interest in establishing the ionization balance for magnetic fusion diagnostics: the closed-subshell case of Sn^{4+} is studied in detail.

3.1. Sn^{11+}

In figure 2, we show the CA results for the total contribution from $\Delta n = 0$ and $\Delta n = 1$ promotions from the ground configuration ($4p^64d^3$).[7] We also show the contribution from the dipole promotions alone, namely 4p–4d plus 4d–4f. We see that the $\Delta n = 1$ contribution is negligible from a plasma modelling perspective—it is at most 10% at the point where the $\Delta n = 0$ contribution has a minimum. We also see that the dipole promotions dominate the $\Delta n = 0$ contribution. Both of these results are in contrast to the behaviour seen for W^{35+} [9]. The difference in charge state explains both trends and they are also seen in L- and M-shell DR: a higher charge state leads to relatively larger radiative rates compared to autoionization

[7] The distinction between $\Delta n = 0$ and $\Delta n = 1$ on energy grounds starts to become blurred at these charge states.

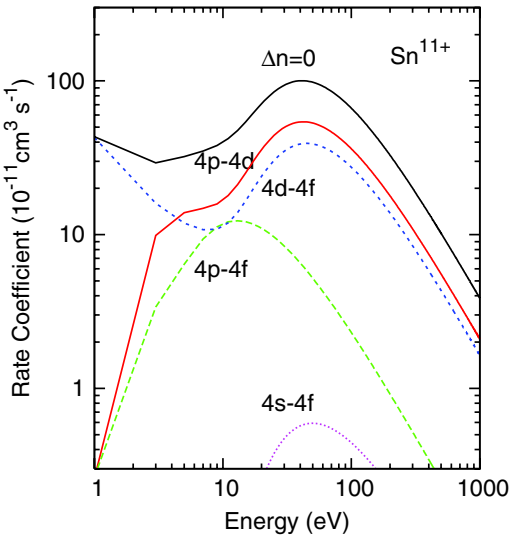

Figure 3. CA $n = 4$–4 DR contributions for Sn^{11+}. $\Delta n = 0$ denotes the sum (l, l') of the $4l$–$4l'$ contributions which are shown individually. (The 4s–4d is off the bottom of the graph—i.e. negligible.) See the text for details. All this work.

as well as to core-excited states supporting more true bound states. In the case of W^{35+}, the non-dipole promotion 4p–4f contributed about a third of the $\Delta n = 0$ contribution because the core radiative stabilization 4f–4d led to true bound states of the form $4p^5 4d^4 nl$ (for $n = 8$–10 depending on l). Fewer such states contribute at lower charge. The net result can be seen in figure 3 where we show the contributions from $4l$–$4l'$. We see that the non-dipole 4p–4f promotion makes a non-negligible contribution only where there is a minimum in the dipole contribution. These relative contributions should be contrasted with those of [9], figure 3. Similar behaviour is seen for the $\Delta n = 1$ promotions shown in figure 4. The dipole promotions 4p–5s and 4d–5p dominate and this is in contrast to that seen for W^{35+}—see [9] figure 5.

We now turn to comparing level-resolved results from AUTOSTRUCTURE with those from the CA. We calculated the 4p–4d and 4d–4f separately first so as to omit the strong configuration-mixing. The question arises then as to which initial levels to average over. In [9] it is argued that it is unlikely that just the ground level is populated in a collisional plasma. Thus, they averaged over all initial levels of the ground configuration and stated that 'this allowed for a direct comparison with the CADW results and also should be more appropriate for modelling'. We agree that excited levels may well have significant populations but it remains to be determined whether they are in any way statistical—except perhaps for the case of the fine-structure levels within a term. It is also hard to say which is more appropriate for comparing with CA. The CA method cannot describe re-autoionization into alternative continua of the ground configuration—there is only one. In the level-resolved case dielectronic capture from the ground level can re-autoionize into progressively excited continua only from increasingly large n. But dielectronic capture from an excited level can always re-autoionize to the continuum of the ground level. The net result is that DR from increasingly excited initial levels is increasingly smaller than that from the ground level. Which is a more meaningful comparison with the CA is not clear.

In figure 5, we present our 'unmixed' 4p–4d and 4d–4f contributions from AUTOSTRUCTURE averaged over just the statistical weight of the ground level as well as for the whole configuration—the former being 50% larger than the latter at the high temperature peak. The CA results for 4p−4d and 4d−4f are 30% and 60% larger than the AUTOSTRUCTURE ones averaged over the initial ground level. They are just over a factor of 2 larger than the AUTOSTRUCTURE results averaged over all levels of the ground configuration. (The large low-temperature contributions have a modest influence of ∼10% at the high-temperature peak. Discounting them slightly increases the CA 'overestimate' since its low temperature

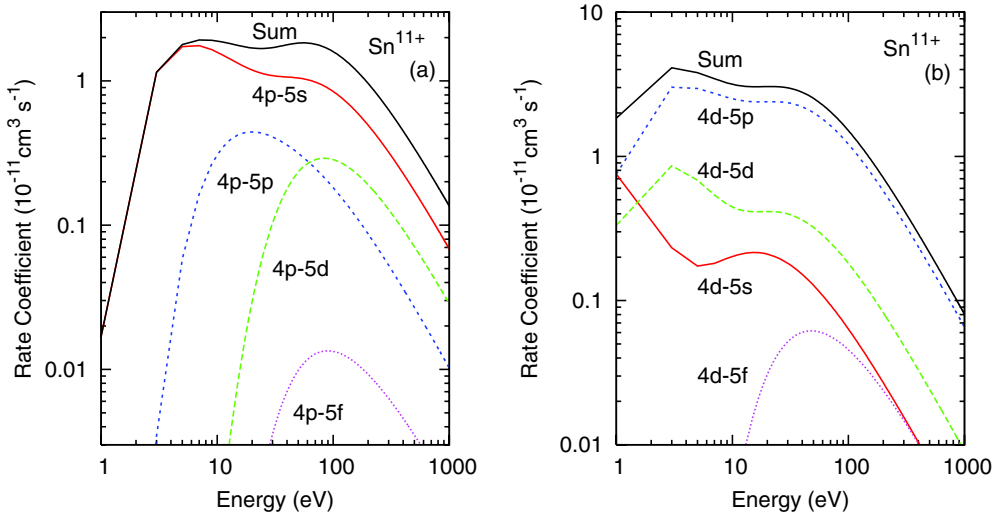

Figure 4. CA DR contributions for Sn^{11+} (a) $n = 4$p–$5l$ and (b) $n = 4$d–$5l$. 'Sum' denotes the sum over l of the 4p, 4d–$5l$ contributions which are shown individually. (The 4p, 4d–5g are off the bottom of the graph.) See the text for details. All this work.

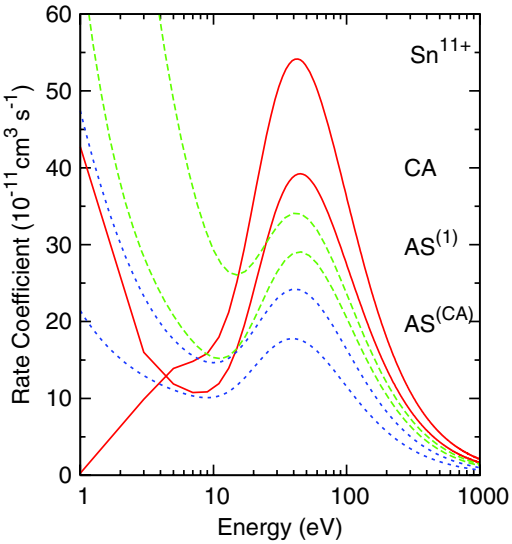

Figure 5. DR 4p–4d and 4d–4f contributions for Sn^{11+}. Solid (red) curves: CA; long-dashed (green) curves: AUTOSTRUCTURE averaged over the initial ground level only; short-dashed (blue) curves: AUTOSTRUCTURE averaged over all levels of the ground configuration. For each pair of curves the upper corresponds to the 4p–4d contribution and the lower one to the 4d–4f contribution. See the text for details. All this work.

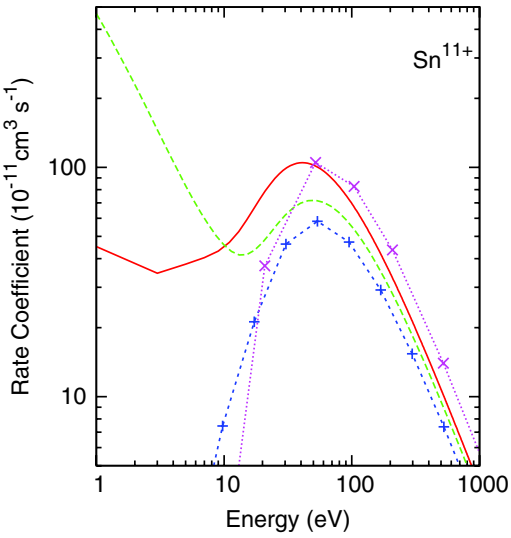

Figure 6. Total DR rate coefficients for Sn^{11+}. Solid (red) curve: CA; long-dashed (green) curve: AUTOSTRUCTURE averaged over the initial ground level; short-dashed (blue) curve: BBGP averaged over the initial ground level; dotted (purple) curve; Burgess GF. All this work.

contribution is smaller.) The closer agreement of the CA results with those for averaging over only the ground level is presumably since this 'minimizes' the suppression by autoionization into excited states. From a modelling perspective we would need to examine the collisional(–radiative) excitation rates so as to determine which of the initial levels were populated significantly. With initial-level-resolved DR data to hand then we can tailor it to the local plasma conditions.

We next consider the inclusion of both dipole promotions in the same AUTOSTRUCTURE calculation. We find a net increase in their total rate coefficient of only 10% at the high-temperature peak compared to summing the two treated separately. This is a combination of the effects of configuration-mixing and the additional autoionization channels between the two excited configurations. Unitarity has a significant role in suppressing differences due to mixing in total rate coefficients. This is less so for the case of final-state resolved partial rate coefficients.

In figure 6, we compare our configuration-mixed level-resolved AUTOSTRUCTURE results with the total rate coefficients from the BBGF and CA methods. The first two sets of results are averaged over the initial ground level and the latter two include all significant promotions. The three sets of results have very different low-temperature contributions. This is not surprising but it slightly complicates comparisons made at the high-temperature peak. We can estimate the contribution for the tin ions considered in this paper as follows based on the relevant scalings with temperature illustrated by equation (1): we take the rate coefficient at ∼10 eV and reduce it by a factor of 10, and then take this to be the estimate of the low-temperature contribution to the high-temperature peak at ∼50 eV. About 8% of the AUTOSTRUCTURE total arises this way while it is negligible for the BBGP and CA results. This 'additional' AUTOSTRUCTURE contribution roughly cancels the contribution from the 'additional' promotions included in the BBGP and CA results over and above the former. Then the CA results are about 45% larger and the BBGP 20% smaller than the AUTOSTRUCTURE results at the high-temperature peak. If we were to average over all levels of the ground configuration, then the CA results would now lie significantly higher than the other two sets—recall figure 5. Results from the Burgess GF are also shown. These were determined using the 4p–4d and 4d–4f oscillator strengths from the configuration-mixed level-resolved AUTOSTRUCTURE target. The peak temperature result is similar to the CA. We note that all results show a large variation at low temperatures. The relevant temperatures of interest for technical plasmas are 30–50 eV while for magnetic fusion plasmas they are somewhat higher at 100–200 eV.

In figure 7, we show the total collisional–radiative DR rate coefficient as a function of electron density as determined using the ADAS *baseline* approach, i.e. the BBGP for DR. Density effects are negligible below $\sim 10^{11}$ cm^{-3}. As the density increases, stepwise ionization reduces the peak rate coefficient by 20% at $\sim 10^{13}$ cm^{-3} and by nearly a factor of 2 at $\sim 10^{15}$ cm^{-3}.

3.2. Sn^{7+}

We find that moving from Sn^{11+} to Sn^{7+} continues the isoelectronic trend noted on comparing and contrasting results for Sn^{11+} to W^{35+}. (The ground configurations $4d^3$ and $4d^7$ are equivalent from an angular momentum coupling perspective.) To illustrate: in figure 8, we show the CA results for the total contribution from $\Delta n = 0$ and $\Delta n = 1$ promotions from the ground configuration. The $\Delta n = 0$ dominate the high-temperature peak and the $\Delta n = 1$ only dominate at very low temperatures because there is no low-temperature contribution

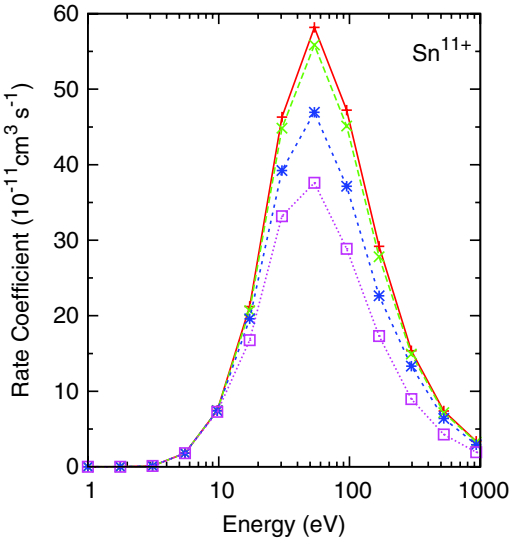

Figure 7. Total DR rate coefficients for Sn^{11+} as a function of electron density. Solid (red) curve: 10^{10} cm^{-3}; long-dashed (green) curve: 4.6×10^{11} cm^{-3}; short-dashed (blue) curve: 2.2×10^{13} cm^{-3}; dotted (purple) curve; 10^{15} cm^{-3}. See the text for details. All this work—see also Foster (2008).

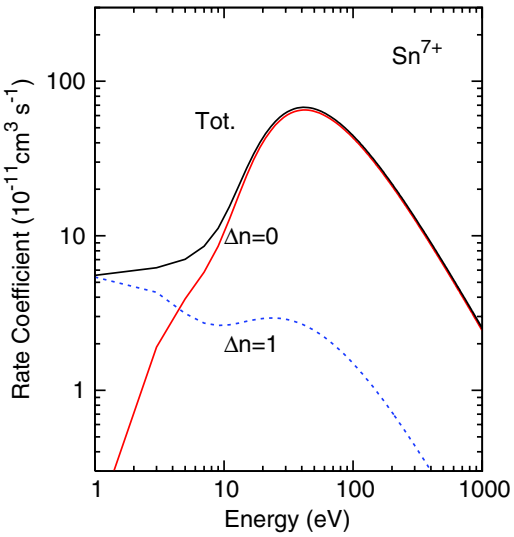

Figure 8. CA DR contributions for Sn^{7+}. $\Delta n = 0$ denotes the sum of the $4l$–$4l'$ contributions and $\Delta n = 1$ denotes the sum of the $4l$–$5l'$. 'Tot.' denotes the sum of the $\Delta n = 0$ plus $\Delta n = 1$. See the text for details. All this work.

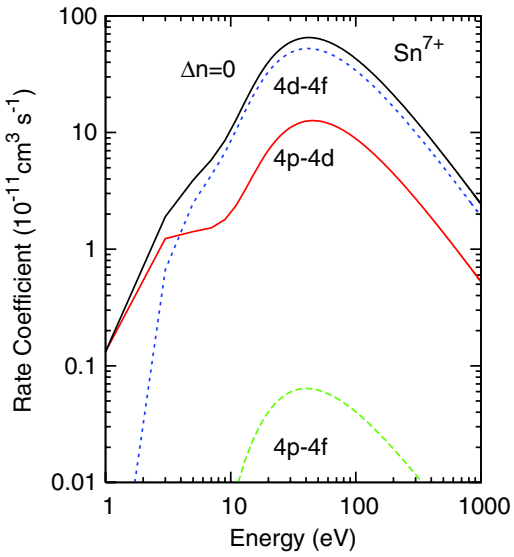

Figure 9. CA $n = 4$–4 DR contributions for Sn^{7+}. $\Delta n = 0$ denotes the sum (l, l') of the $4l$–$4l'$ contributions which are shown individually. (The 4s–$4l$ are off the bottom of the graph.)

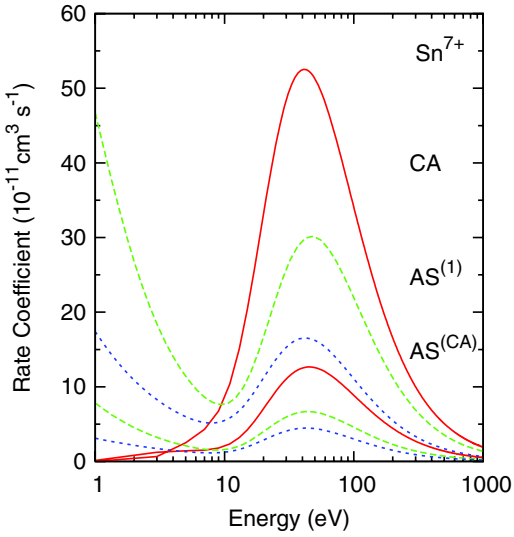

Figure 10. DR 4p–4d and 4d–4f contributions for Sn^{7+}. Solid (red) curves: CA; long-dashed (green) curves: AUTOSTRUCTURE averaged over the initial ground level only; short-dashed (blue) curves: AUTOSTRUCTURE averaged over all levels of the ground configuration. For each pair of curves the lower corresponds to the 4p–4d contribution and the upper one to the 4d–4f contribution. See the text for details. All this work.

associated with the $\Delta n = 0$ promotion for this ion. Within the $\Delta n = 0$ contributions the dipoles are now completely dominant—see figure 9—and the same is true for $\Delta n = 1$ (not shown).

In figure 10, we compare our unmixed 4p–4d and 4d–4f results from AUTOSTRUCTURE with those from the CA. The CA results are already around 80% larger than those from AUTOSTRUCTURE averaged over the ground level. Averaging over all initial levels of the ground configuration increases the difference to about a factor of 3.

In figure 11, we compare our configuration-mixed level-resolved AUTOSTRUCTURE results with the total rate coefficients from the BBGP and CA methods. The configuration-mixed AUTOSTRUCTURE result is only 5% smaller than the sum of the unmixed results (not shown) at the high-temperature peak. The BBGP results are again somewhat smaller than our ones from AUTOSTRUCTURE. They also show a large low-temperature contribution which somewhat improves the agreement with the AUTOSTRUCTURE results at the high-temperature peak. The BBGP results are ∼30% smaller than the AUTOSTRUCTURE ones on making an allowance for this contribution. The low-temperature variation of the rate coefficients is likely due to the 'random' positioning of near-threshold resonances. Our unmixed AUTOSTRUCTURE results in

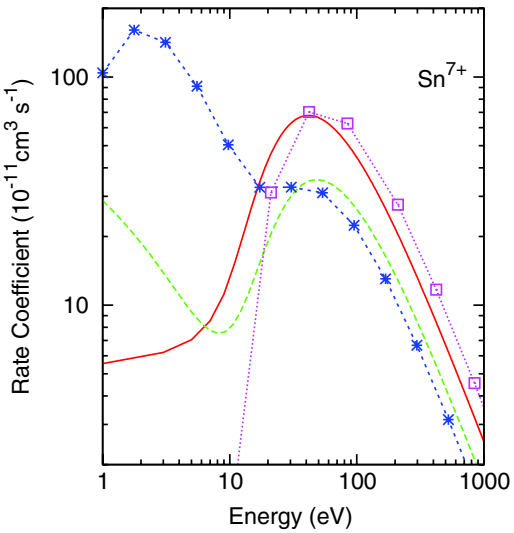

Figure 11. Total DR rate coefficients for Sn^{7+}. Solid (red) curve: CA; long-dashed (green) curve: AUTOSTRUCTURE averaged over the initial ground level; short-dashed (blue) curve: BBGP averaged over the initial ground level; dotted (purple) curve; Burgess GF. All this work.

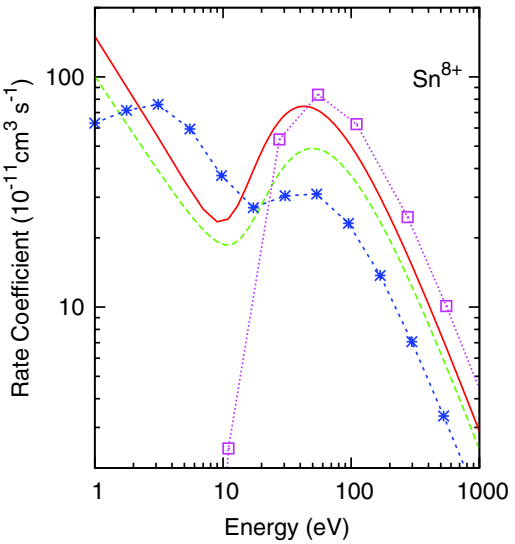

Figure 12. Total DR rate coefficients for Sn^{8+}. Solid (red) curve: CA; long-dashed (green) curve: AUTOSTRUCTURE averaged over the initial ground level; short-dashed (blue) curve: BBGP averaged over the initial ground level; dotted (purple) curve; Burgess GF. All this work.

figure 10 show a comparably large contribution but peaked at a lower temperature. The CA results have a negligible low-temperature contribution and are nearly a factor of 2 larger than the AUTOSTRUCTURE results at the high-temperature peak and are only a marginal improvement over the results of the Burgess GF here.

3.3. Sn^{8+}–Sn^{10+}

In figures 12–14, we compare our configuration-mixed level-resolved AUTOSTRUCTURE results with the total rate coefficients from the BBGP method for Sn^{8+}, Sn^{9+} and Sn^{10+}, respectively. We compare also with CA results obtained from including just the 4p–4d and 4d–4f promotions now. These are the same promotions as included in the AUTOSTRUCTURE and Burgess GF results.

3.3.1. Sn^{8+}. The AUTOSTRUCTURE, BBGP and CA results all have similar low-temperature contributions. The BBGP results lie 40% below, the CA 55% above and the GF 80% above the AUTOSTRUCTURE ones.

3.3.2. Sn^{9+}. The very large low-temperature contribution in the AUTOSTRUCTURE results pushes the high-temperature peak (in as much as there is one) close to that of the Burgess GF. We estimate the 'low-temperature' contribution to be nearly half of the total at 50 eV. If we attempt to factor that out, then the BBGP results are roughly 45% lower and the CA 45% higher—but clearly this is roughly. The Burgess GF results are again only a little larger than the CA ones here.

3.3.3. Sn^{10+}. The pattern of results here is similar to those just discussed for Sn^{9+}. The BBGP results are roughly 15% lower and the CA 50% higher than the AUTOSTRUCTURE ones if we attempt to compensate for the 'low-temperature' contribution

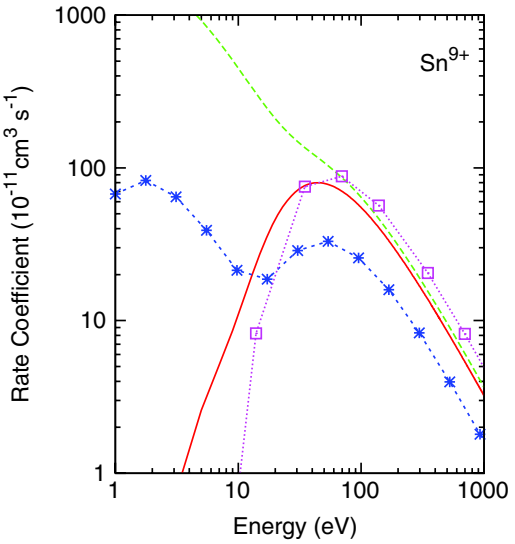

Figure 13. Total DR rate coefficients for Sn^{9+}. Solid (red) curve: CA; long-dashed (green) curve: AUTOSTRUCTURE averaged over the initial ground level; short-dashed (blue) curve: BBGP averaged over the initial ground level; dotted (purple) curve; Burgess GF. All this work.

at 50 eV. We also show the results obtained from the FAC [5]. They have a modest low-temperature contribution which is comparable to the CA one. The FAC results are about 30% lower than the 'compensated' AUTOSTRUCTURE ones. The FAC calculations should be the closest to the AUTOSTRUCTURE ones. The 30% difference is perhaps a little large given the insensitivity to atomic structure or at least configuration-mixing. The FAC approach [6] solves the Dirac equation self-consistently using a unique model potential which is basically a weighted average of the CA potentials 'seen' by each orbital, i.e. excluding self-interaction. This maintains orthogonality of the orbitals. We do not carry out this second average

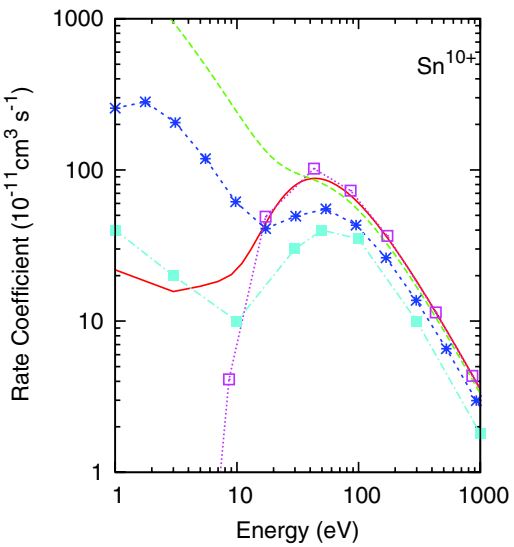

Figure 14. Total DR rate coefficients for Sn^{10+}. Solid (red) curve: CA; long-dashed (green) curve: AUTOSTRUCTURE averaged over the initial ground level; short-dashed (blue) curve: BBGP averaged over the initial ground level; dotted (purple) curve; Burgess GF: all this work. Dot-dashed (cyan) curve, FAC results from [5].

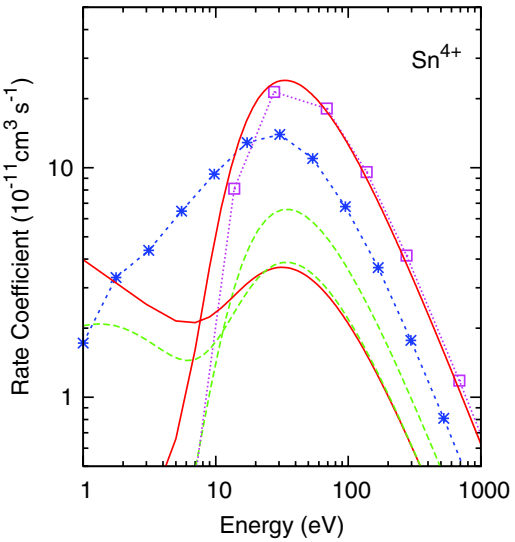

Figure 15. Total DR rate coefficients for Sn^{4+}: where there are pairs of curves the lower/upper are with/without $n = 5$ (see the text). Solid (red) curves: CA; long-dashed (green) curves: AUTOSTRUCTURE averaged over the initial ground level; short-dashed (blue) curve: BBGP averaged over the initial ground level; dotted (purple) curve; Burgess GF. All this work.

but instead follow Cowan [21] in neglecting the overlap contributions. Our use of the kappa-averaged relativistic wavefunctions should be sound for these outer-shell orbitals. A very accurate description of the atomic structure of Sn^+ has been obtained using only non-relativistic wavefunctions [25].

3.4. Sn^{12+} and Sn^{13+}

As we approach the shell boundary, the complexity of the angular momentum coupling problem simplifies and becomes computationally less demanding. There may be additional complexities in describing the structure on breaking a closed shell or the polarization of a single electron outside of a closed shell, but they are beyond the scope of this work. The shell boundary (Kr-like here) is important in plasma modelling since such ions are relatively more abundant over a wide temperature range.

Results (not shown) for the high-charge ions Sn^{12+} and Sn^{13+} show variable low-temperature contributions similar to those seen for Sn^{11+}. The Burgess GF results are about 30% larger than those from AUTOSTRUCTURE at the high-temperature peak while the CA results are about 25% larger but those from the BBGP are nearly a factor of 2 smaller.

3.5. Sn^{4+}–Sn^{6+}

The 'simple' picture of $\Delta n = 0$ and $\Delta n = 1$ transitions/promotions breaks down at low charges. Levels of the $4d^{(q-1)}5l$ configurations increasingly move below those of the $4d^{q-1}4f$. This has two consequences. Rydberg states associated with the 4d–4f promotion now become increasingly energetically accessible to the 5s, then 5p, and finally the 5d continua. We expect the AUTOSTRUCTURE level-resolved autoionization rates associated with the 4d–4f promotion to dominate over 4f–5p and especially 4f–5s, but there will be some suppression still. This is expected to be offset to a degree by the increasing direct contribution from $\Delta n = 1$ promotions as they are no longer energetically accessible to the 4f continua.

The use of the CA method becomes increasingly problematic here. Levels of the $4d^{(q-1)}4f$ target/parent configuration become increasingly intermixed with those of the $4d^{(q-1)}5l$. The CA method 'requires' that *all* levels of $4d^{q-1}4fnl$ be above or below $4d^{(q-1)}5s$, 5p etc. This is impossible to satisfy in the high-n limit when the parents are intermixed. The 'high-n' limit becomes not so high at low charge. We illustrate this in the following section.

3.5.1. Sn^{4+}. The closed-subshell $4d^{10}$ no longer admits the 4p–4d promotion and its consequential mixing with that arising from the 4d–4f promotion. It is a rather pure system. There is a single strong completely dominant $\Delta n = 0$ radiative rate from the $4d^9 4f\ ^1P_1$ level and this is the highest lying level in the configuration. The associated 4f-wavefunction is strongly term dependent.

In figure 15, we compare the total DR rate coefficients for Sn^{4+} obtained from the various methods. We present pairs of results for AUTOSTRUCTURE and CA. One set is simply the result from including $n = 4$ target configurations (i.e. $\Delta n = 0$ promotions). The second set includes $n = 5$ target configurations. The effect of the latter is quite complex.

We see that the $n = 4$ AUTOSTRUCTURE results lie substantially below the equivalent CA ones as well as the BBGP and Burgess GF. We interpret this as follows: Rydberg nl states attached to the $4d^9 4f\ ^1P_1$ core can autoionize into the continuum of lower levels of the $4d^9 4f$ configuration for $n > 5$. This strongly suppresses the DR in this simple system. If we omit such autoionization channels from our AUTOSTRUCTURE calculation, then the peak temperature rate

coefficient increases by nearly a factor of 2. Such non-dipole autoionizing transitions within a configuration are not described by either the BBGP or CA methods.

We can investigate the effect of the $4d^9 5l$ configurations which (for $l = 0$–2) lie wholly ($l = 0, 1$) or partially ($l = 2$) below the $4d^9 4f$. We find that their inclusion reduces the AUTOSTRUCTURE result for the peak temperature rate coefficient by only 5%. The reasons for this are twofold. The suppression of the DR via the 4d–4f promotion by autoionization into the $n = 5$ continua has to compete against the suppression via 4f–4f which is already included. Then there is a contribution to DR from the 4d–5p promotions which is only suppressed by autoionization into the 5s continuum. The two effects each affect the total rate coefficient by roughly 20–30% but are largely self-cancelling. Both effects are diminished in magnitude as the charge state increases.

The situation for the CA method is dramatically different. The inclusion of autoionization into the $n = 5$ continua reduces the 4d–4f peak temperature rate coefficient by about a factor of 12. The $\Delta n = 1$ contribution is then comparable with the reduced $\Delta n = 0$ and in contradistinction to the AUTOSTRUCTURE finding. This partially offsets the effect of the dramatic suppression of the 4d–4f contribution to the total. The net result is a factor of 7 reduction of the CA total peak temperature rate coefficient which is in turn about a factor of 2 smaller than the ($nl = 5s - 5d$) AUTOSTRUCTURE result (not shown—see next).

We now turn to term dependence. The $4d^9 4f\ ^1P_1 \rightarrow 4d^{10}\ ^1S_0$ radiative rate from the $n = 4$ AUTOSTRUCTURE target is broadly comparable with the CA value: 3.3×10^{11} s^{-1} versus 2.3×10^{11} s^{-1}. We use Fischer's Hartree–Fock code [26] to obtain a term-dependent $4f\ ^1P$ wavefunction: the radiative rate is 6.6×10^{10} s^{-1}. We can attempt to correct for term dependence in the AUTOSTRUCTURE calculation by including the $4d^9 5f$ configuration. This results in a rate of 9.5×10^{10} s^{-1} from the $4d^9 4f\ ^1P_1$. This factor 3 reduction translates into a 40% reduction in the peak temperature DR rate coefficient as the reduction of the 4f contribution due to term dependence is partially offset by the (enhanced) contribution from the 5f promotion.

There is no configuration mixing in the CA method and so no account is taken of term dependence. The final term-dependent corrected AUTOSTRUCTURE peak temperature DR rate coefficient lies remarkably and likely coincidentally close (10%) to the CA one perhaps indicating the overall effect of unitarity on the totals.

3.5.2. Sn^{5+} and Sn^{6+}. Results (not shown) for these two ions show a similar trend to those seen for Sn^{7+}. The BBGP results differ by 5% and 20% respectively from the AUTOSTRUCTURE results at the high-temperature peak while those of the Burgess GF and CA (without $n = 5$) are a factor of 2 larger. The low-temperature results for these ions are reduced both in relative magnitude and variation compared to those already presented for Sn^{7+}. If we include the $4d^9 5l$ configurations ($l = 0$–2), we find that our AUTOSTRUCTURE result for the peak temperature rate coefficient changes by only 1%. (There are larger low-temperature effects due to the change in the position of near threshold resonances because of the change in the configuration interaction expansion.)

The situation for the CA improves with the increased charge but this is likely simply due to the importance of the fundamental effect itself decreasing as the standard ordering of 4f and 5*l* re-asserts itself. This reduces and then eliminates the $n = 5$ continua suppression effect on DR via the $4d - 4f$ promotion and in turn causes the $4d - 5p$ contribution to the recombination itself to be suppressed increasingly by autoionization into excited states. Inclusion of the $n = 5$ suppression of the $\Delta n = 0$ contribution reduces the net high-temperature peak total rate coefficient by a factor of 4 for Sn^{5+} and 40% for Sn^{6+}. This 40% reduction for Sn^{6+} brings the CA result into good agreement (15%) with our AUTOSTRUCTURE result but it is coincidental. The contribution from $\Delta n = 1$ promotions in their own right is now about 20% of the total for Sn^{5+}.

We have not included the $n = 5$ suppression effect in the CA $\Delta n = 0$ results presented for other ions. (Where a $\Delta n = 1$ contribution is shown it was calculated separately.) We note here that the Sn^{7+} total peak temperature rate coefficient is reduced by 25% if included. We recall that our AUTOSTRUCTURE result is reduced by nearly a factor of 2 if we choose to average over all levels of the ground configuration as opposed to just the ground level. The variation in the CA results should be seen in this perspective.

3.6. Fitting coefficients

It is convenient often for simple modelling purposes to fit the total DR rate coefficient to the following functional form:

$$\alpha^z(T) = T^{-3/2} \sum_i c_i \exp\left(\frac{-E_i}{T}\right) \qquad (2)$$

where the E_i are in the units of temperature T (e.g. eV) and the units of c_i are then cm^3 s^{-1}(eV)$^{3/2}$.

In table 1, we present the fitting coefficients for our AUTOSTRUCTURE total DR rate coefficients for the initial ground level of Sn^{z+} (for $z = 4$–13) which are based upon the functional form given by equation (2). The fits are accurate to better (often much better) than 5% over 1–1000 eV.

The total DR rate coefficients can be taken to be the total recombination rate coefficients. The contribution from radiative recombination is negligible over the given temperature range as is that from three-body recombination at the densities of interest to technical and magnetic fusion plasmas.

4. Recapitulation

We have made extensive calculations of DR rate coefficients for Sn^{z+} ($z = 4$–13) ions using configuration-mixed Breit–Pauli, Burgess–Bethe and CA methods. If we except the special case of the closed-subshell Sn^{4+} ion, then we can state some broad findings.

(i) Dipole $\Delta n = 0$ promotions dominate. This behaviour is in contrast to that found for W^{35+} [9] (which is

Table 1. Total DR rate coefficient fitting coefficients c_i (cm^3 s^{-1} (eV)$^{3/2}$) and E_i (eV) for the initial ground level of Sn^{z+}.

z	c_1	c_2	c_3	c_4	c_5
13	5.658(−10)[a]	8.904(− 9)	2.214(− 8)	1.298(− 7)	1.409(− 6)
12	1.346(− 9)	4.586(− 9)	1.654(− 8)	1.229(− 7)	1.188(− 6)
11	2.778(− 9)	5.772(− 9)	6.306(− 9)	1.144(− 7)	1.130(− 6)
10	1.770(− 8)	2.561(− 8)	5.012(− 8)	2.031(− 7)	8.360(− 7)
9	1.072(− 8)	1.000(− 7)	9.232(− 8)	8.136(− 7)	2.250(− 7)
8	3.346(−10)	1.022(− 9)	2.660(− 9)	2.276(− 8)	7.998(− 7)
7	5.242(−11)	2.498(−10)	9.592(−10)	6.862(− 9)	5.566(− 7)
6	3.541(−11)	6.719(−11)	1.749(− 9)	3.416(− 7)	6.493(− 8)
5	2.748(−12)	4.578(−12)	5.032(−10)	1.692(− 7)	6.514(− 8)
4	2.054(−10)	9.896(−10)	4.259(− 8)	2.052(− 8)	2.190(−10)
z	E_1	E_2	E_3	E_4	E_5
13	1.654(− 1)	2.011(0)	8.695(0)	4.152(+ 1)	9.022(+ 1)
12	1.717(− 1)	1.413(0)	6.970(0)	4.062(+ 1)	8.971(+ 1)
11	1.331(− 1)	9.384(− 1)	6.094(0)	3.834(+ 1)	8.997(+ 1)
10	8.116(− 2)	9.333(− 1)	4.000(0)	4.602(+ 1)	9.643(+ 1)
9	2.731(− 1)	2.110(0)	6.049(0)	7.407(+ 1)	1.340(+ 2)
8	7.158(− 2)	5.526(− 1)	3.232(0)	2.054(+ 1)	8.255(+ 1)
7	5.997(− 2)	4.930(− 1)	2.406(0)	1.776(+ 1)	7.715(+ 1)
6	1.958(− 1)	1.385(0)	1.275(+ 1)	6.674(+ 1)	1.195(+ 2)
5	1.047(− 1)	8.616(− 1)	1.245(+ 1)	5.718(+ 1)	9.505(+ 1)
4	2.493(0)	1.611(+ 1)	5.145(+ 1)	6.909(+ 1)	2.379(+ 3)

[a] (m) denotes $\times 10^m$.

isoelectronic with Sn^{11+}) where both non-dipole and $\Delta n = 1$ promotions made notable contributions. It is readily understood in terms of the z-scaling of the relevant energies and rates.

(ii) Configuration-mixing between $4p^6 4d^{(q-1)} 4f$ and $4p^5 4d^{(q+1)}$ has a small effect on the total DR rate coefficient. This is despite the significant effect it has on individual radiative rates for example. Unitarity dominates.

(iii) The BBGP results are systematically lower than those obtained from AUTOSTRUCTURE. In some cases they are significantly lower (by a factor of 2).

(iv) The CA results are systematically and significantly higher (by up to a factor of 2) than the configuration mixed Breit–Pauli results obtained from AUTOSTRUCTURE. Their improvement over results obtained from the Burgess GF is marginal at best. This is in contrast to that found previously for W^{35+} [9] and appears to be due to the lower residual charge here. Caveat: at the lowest charges the $\Delta n = 0$ CA results are reduced significantly by including autoionization to the $n = 5$ continua. This is only partially offset by the $\Delta n = 1$ contribution. The net effect is only a few percent effect in the fully level-resolved picture described by AUTOSTRUCTURE.

(v) The AUTOSTRUCTURE results differ significantly (by up to 70%) between averaging over just (the weight of) the ground level and all levels of the ground configuration.

5. Conclusions

The BBGP and CA methods should be used to determine the dominant promotions which contribute to the DR processes of interest for heavy species. They can be used also to 'top-up' small contributions. The BBGP method may be preferable since it describes N-electron configuration-mixing and it can resolve by initial level—this latter feature is especially important at low charge. But the CA method may still be required so as to assess the importance of non-dipole promotions since the BBGP method requires externally sourced distorted wave collision strengths to describe them. A full level-resolved treatment appears to be necessary for the dominant contributions so as to obtain totals accurate to better than a factor of 2 compared to the more approximate BBGP and CA methods. The full configuration-mixed Breit–Pauli implementation within the AUTOSTRUCTURE code can describe such DR processes involving a half-open d-subshell. A complete set of such results for tungsten ions is highly desirable. (Recall that the agreement between AUTOSTRUCTURE and CA for W^{35+} was obtained by averaging over all levels of the initial ground configuration [9].) The f-subshell will be the next challenge. This is necessary for describing DR processes in the tungsten ions: W^{13+} – W^{27+}. It is likely that the BBGP and/or CA methods will have to play a greater role then.

Acknowledgment

This work was supported in part by a Euratom Framework 7 Support Action agreement with the University of Strathclyde.

References

[1] Bakshi V (ed) 2006 *EUV Sources for Lithography* (*SPIE Press Monograph* vol PM149) (Bellingham, WA: SPIE Press)

[2] White J, Hayden P, Dunne P, Cummings A, Murphy N, Sheridan P and O'Sullivan G 2005 *J. Appl. Phys.* **98** 113301

[3] Bauche J, Bauche-Arnault C and Klapisch M 1987 *Adv. At. Mol. Phys.* **23** 131–95

[4] Bauche J, Bauche-Arnault C, Klapisch M, Mandelbaum M and Schwob J-L 1987 *J. Phys. B: At. Mol. Phys.* **20** 1443–50
[5] Fu Y-B, Dong C-Z, Su M-G and O'Sullivan G 2007 *Chin. Phys. Lett.* **25** 927–9
[6] Gu M F 2008 *Can. J. Phys.* **86** 675–89
[7] ITER Physics Basis 1999 *Nucl. Fusion* **39** 2137–74
[8] Foster A 2008 *PhD Thesis* University of Strathclyde
[9] Ballance C P, Loch S D, Pindzola M S and Griffin D C 2010 *J. Phys. B: At. Mol. Opt. Phys.* **43** 205201
[10] Badnell N R 2011 *Comput. Phys. Commun.* **182** 1528–35
[11] Badnell N R, Berrington K A, Summers H P, O'Mullane M G, Whiteford A D and Ballance C P 2004 *J. Phys. B: At. Mol. Opt. Phys.* **37** 4589–601
[12] Sterling N C, Dinerstein H L and Kallman T R 2007 *Astrophys. J. Suppl. Ser.* **169** 37–61
[13] Burgess A 1964 *Astrophys. J.* **139** 776–80
[14] Summers H P 2004 *The ADAS User Manual v2.6* http://www.adas.ac.uk
[15] Burgess A 1965 *Astrophys. J.* **141** 1588–90
[16] Badnell N R, O'Mullane M G, Summers H P, Altun Z, Bautista M A, Colgan J, Gorczyca T W, Mitnik D M, Pindzola M S and Zatsarinny O 2003 *Astron. Astrophys.* **406** 1151–65
[17] Badnell N R 1986 *J. Phys. B: At. Mol. Phys.* **19** 3827–35
[18] Eissner W, Jones M and Nussbaumer H 1974 *Comput. Phys. Commun.* **8** 270–306
[19] Badnell N R 2006 *J. Phys. B: At. Mol. Opt. Phys.* **39** 4825–52
[20] Cowan R D and Griffin D C 1975 *J. Opt. Soc. Am.* **66** 1010–4
[21] Cowan R D 1981 *The Theory of Atomic Structure and Spectra* (Berkeley, CA: University of California Press)
[22] Griffin D C, Pindzola M S and Bottcher C 1985 *Phys. Rev.* A **31** 568–75
[23] Pindzola M S, Griffin D C and Bottcher C 1986 *Atomic Processes in Electron–Ion and Ion–Ion Collisions* (*NATO ASI* B vol 145) (New York: Plenum) pp 75–91
[24] Cowan R D and Griffin D C 1987 *Phys. Rev.* A **36** 26–32
[25] Oliver P and Hibbert A 2010 *J. Phys. B: At. Mol. Opt. Phys.* **43** 074013
[26] Froese Fischer C 1991 *Comput. Phys. Commun.* **64** 369–98